



ALMA MATER STUDIORUM
UNIVERSITÀ DI BOLOGNA

DEPARTMENT OF INDUSTRIAL ENGINEERING
Forlì Campus

Bachelor's Degree in
INGEGNERIA AEROSPAZIALE
Class L-9

**Development of a code for the measurement of
aerodynamic friction drag on arbitrary
geometries with the OFI optical technique**

FINAL DEGREE THESIS
in
Aircraft Aerodynamics

Supervisor:
Prof. Gabriele Bellani

Defended by:
Nicola del Zingaro

December 2023 Session
Academic Year 2022/2023

Acknowledgements

I thank my supervisor, Prof. Gabriele Bellani, for his support and advice in writing this thesis. I too thank his collaborators and my aerodynamics professor for his passion in conveying the subject.

I thank my family for being themselves.

I thank all those who made me grow into who I am today and that I always carry with me.

Abstract

This thesis aims at analyzing different viable procedures for the implementation of the OFI skin friction measurement technique and identifying among them the one best suitable to obtaining precise, accurate and the least possible time consuming shear stress evaluations at arbitrary points of a test surface, whose geometry may not be a priori known. Thereafter, the focus of the thesis shifts to the development of a code, which, according to the studied possibilities, allows for estimating skin friction on an arbitrary surface for a given set of OFI test data.

Contents

Introduction	9
1 Background: Oil Film Interferometry	14
1.1 Theory	14
1.2 Experimental Setup	15
1.2.1 Test Surface	15
1.2.2 Oil	15
1.2.3 Camera	15
1.2.4 Lighting Source	15
1.3 The Procedure	16
1.3.1 Calibration	16
1.3.2 Experimental Data Analysis	16
2 Implementation of OFI over Arbitrary Surfaces	20
2.1 Theory	20
2.2 Experimental Setup	21
2.2.1 The Checkerboard	22
2.2.2 The Model	22
2.2.3 Thermocouple and Dynamic pressure probe	23
2.3 The Procedure	23
2.3.1 Experimental Data Analysis	24
3 Test Case and Validation	29
3.1 Theoretical Results	29
3.2 Data Presentation	31
3.3 The Procedure	32
3.3.1 Camera Calibration	33
3.3.2 Image Processing and Calculations	40
4 Results	46
5 Conclusions	52

Introduction

Nowadays, environmental issues and sustainable development represent some of the most inspected themes when it comes to engineering applications. This also applies to the field of fluid dynamics. Reducing the environmental impact and fuel consumption of ground vehicles and aircraft at low and high Mach numbers, optimizing the behaviour of flows in ducts, being them gas or liquid, or around buildings and structures are some of the main practical demands fluid dynamics and aerodynamics specialists are faced with in the modern era.

In this regard, the reduction of aerodynamic drag assumes a dominant role. At low Mach numbers, drag mainly accounts for two distinguished components: form drag and skin friction. Form drag mainly depends on the characteristics of the wake a body leaves behind itself when it moves through a fluid. The wake is originated when the flow separates¹ from the body's surfaces and the earlier separation occurs, the larger is the wake, generally. Indeed, early separation can determine very low pressure in the body's base, i.e. the area of the surface enclosed by the separation lines. This low pressure induces an aerodynamic force in the direction of the relative wind opposing the body's forward motion. On the other hand, aerodynamic skin friction generates at the interface between bodies and the air domain due to the no-slip boundary condition, then, to the microscopic imperfections of body surfaces: the number of air molecules hitting the walls' asperities and casually bouncing back, with no preferential direction nor speed intensity, is so large that the phenomenon can be considered statistically stable and the mean velocity of particles at domain boundaries zero in all directions. Being air a "Newtonian fluid", i.e. a fluid which obeys Stokes' friction law, wall tangential stress on a body submerged in air, i.e. aerodynamic friction, is proportional to the velocity gradient at the wall through a constant value μ , called dynamic viscosity of the fluid.

An air flow can be laminar or turbulent. Transition from one state to the other is one the most studied problems in fluid dynamics still today. A turbulent boundary layer is more energetic than a laminar one and is endowed

¹A flow is said to separate from a body when its velocity gradient's component orthogonal to the surface at the wall equals zero, namely when the positive pressure gradient along the body's edge is so large that the particles closer to the surface get slowed down until their speed is null and they then get pushed away.

with a diffusivity level at least two orders of magnitude larger. This determines a turbulent boundary layer’s velocity profile to be much more inclined at walls than a laminar one, since the kinetic energy of particles closer to the surface is replenished by flow particles incoming from the flow’s core. That is to say a TBL exhibits higher velocity close to walls, meaning the tangential stress it causes is more consistent too. Despite being the source of higher friction, for the same reasons, turbulence provides the boundary layer with sufficient energy to avoid separation for longer than a laminar one would. So, a laminar flow might as well be the source of higher form drag.

These observations point out the importance of predicting the location of laminar-turbulent boundary layer transition (Gluzman et al. (2022); Von Karman (1934); Dong et al. (2018)) and controlling separation (Gluzman et al. (2022); Wadcock et al. (1999); Liu (2019)), when the goal is understanding aerodynamic drag.

Oil film interferometry (OFI) is a direct optical technique used in fluid dynamics studies to measure aerodynamic skin friction drag. It has been existing and used for decades, but still up to this day it constitutes one of the most accurate and less invasive methodologies to estimate surface stress at walls experimentally. OFI makes it possible to reach percent errors lower than 1%, whereas alternative strategies yield sensitively larger errors (e.g.: around 4%), as reported by Vinuesa et al. (2017). OFI measurements can be used to complement DNS and CFD simulation results: these tools cannot always foreshadow the development of a real flow when three-dimensional effects (that are capable of generating unusual conditions such as ”backflows”) are involved and may not be fully able to accurately predict the flow’s transition behaviour. Instead, OFI works correctly in these situations, being an experimental technique.

One example of an alternative method to OFI is the pressure drops method, a technique which enables carrying out an indirect measure of wall tangential stress through the evaluation of the pressure gradient ∇p along the axis of the flow. However, it should be noted that this is only possible for inner flows such as pipe or channel flows, as in the case of the CICLoPE Long pipe² wind

²The CICLoPE facility is a research laboratory, born to study high Reynolds number turbulent flows, which allows for some of the best space and time resolved measurements in turbulent pipe flows in the world. CICLoPE’s Long pipe duct makes it possible for achieving high resolution measurements at Reynolds numbers much higher than those at which similar facilities are capable of attaining the same level of accuracy.

tunnel, which was employed for the purposes of this thesis. The main limit of the pressure drops method is represented by the high uncertainty of the measurement instruments when the flow's speed is too low. Due to the small pressure gradient assessable in these conditions, the pressure measuring devices yield imprecise results. OFI does not account for such constraints and can therefore be implemented for any value of ∇p . Besides, OFI makes it possible to realize aimed measurements, related to specific points of a surface, unlike other techniques such as this.

Thus far, the OFI technique has been largely employed for measuring skin friction on plane geometries. OFI implementation becomes more complex if one gets to apply the technique to three-dimensional surfaces. First of all, due to the traction of oil to the wall, the fringes of the "interferometric pattern" which generates onto a curved surface are deformed differently than they would be if they were to be produced on a flat surface and this poses a problem in accurately determining the distancing between consecutive fringes. Secondly, the fact that the surface exhibits a curvature makes it harder to compute, for an examined point of it, the incidence angle of the light rays hitting it. This knowledge is necessary to evaluate the friction coefficient Cf , purpose of the method. To obtain it, it would be necessary to precisely know, mathematically, the analysed geometry and the position of the camera acquiring the pictures of the interferometric pattern, which represents a very bounding aspect. In case the geometry of the analysed surface was not known, it would be possible to reconstruct it via a "cartesian modelling" process, long and tedious.

The present thesis is divided in three main parts:

- Chapter 1 and 2 are dedicated to the exposure of two alternative methods for the implementation of OFI. The first one is the reference procedure employed at the CICLoPE laboratory (University of Bologna) in the last years, on a flat geometry; secondly, an alternative procedure is presented, mainly derived from the one described in Gluzman et al. (2022) and exploiting sharp photogrammetry expedients to obtain skin friction measurements over 3D not a priori known surfaces;
- Chapter 3's first part consists of a comparison between the two methodologies exposed, pointing out their own advantages and differences. Then, a Matlab numerical algorithm for the analyses of a given set of OFI data, obtained at CICLoPE in march/april 2023, and resulting

from the combination of the two described techniques is gone through and explained;

- Chapter 4 contains the analysis of the obtained results, whose achievement had to undergo some not negligible assumptions. The results are compared with empirical curves and data coming from scientific literature. Some final considerations and remarks conclude the text, along with advices for future experiments.

1 Background: Oil Film Interferometry

This is the main modality adopted until today for the implementation of Oil Film Interferometry at the CICLoPE laboratory. It is suitable for the application to flat surfaces; in CICLoPE it is employed inside a "pipe" duct.

1.1 Theory

The technique is based on the mathematical formulations by Tanner and Blows (1976) and Squire (1961), to whom we owe the thin oil film equation, which describes the motion of a thin oil film undergoing shear stress:

$$\frac{\partial h_{oil}}{\partial t} + \frac{\partial}{\partial x} \left(\frac{\tau_w h_{oil}^2}{2\mu_{oil}} \right) = 0 \quad (1.1)$$

From the integration of this and after re-deriving the result with respect to x , an expression for the derivative of h_{oil} , the oil film thickness, with respect to x , coordinate representing the deformation direction of the oil drop, is obtained, as a function of the wall shear stress τ_w . Joining this to a series of observations around the optical path carried out by the light rays emitted by the light source and captured by the camera, the following expression for aerodynamic friction τ_w is finally secured:

$$\tau_w = \frac{\mu_{oil}}{\Delta h_{oil}} \frac{\Delta x}{t} \quad (1.2)$$

, where Δx represents the variation of spacing between the interferometric fringes that can be observed between the generic time instant t and time instant $t_0(t = 0)$, namely the one at which the first value of the fringe spacing x was sampled (the instant of acquirement of the first picture of the interferometric pattern). Δh_{oil} is the difference between the thicknesses of two consecutive oil fringes and it be proved to be constant along the film's length. Incidentally, this means the oil drop stretches maintaining a wedged shape.

1.2 Experimental Setup

1.2.1 Test Surface

The test surface over which the oil drop is applied should present good reflecting capabilities, in order to attain an appropriate visualisation of the interferometric pattern. Good reflecting capabilities usually go along with a sufficiently high refractive index, tending to 2. Examples of suitable materials in this sense are SF11 glass (1.78), Kapton (around 1.50) or Mylar (1.67). The test surface shall be prepared by placing over it a piece of one of these materials.

1.2.2 Oil

It is fundamental for the viscosity of the oil employed to be the less possible sensitive to temperature variations. Thanks to their insensitivity to temperature oscillations, silicon oils are largely used for the implementation of OFI, e.g. the "Dow Corning 200" oil.

1.2.3 Camera

The choice of the camera is arbitrary. One might prefer to a high resolution camera, so as to gather more accurate results. Nikon and Canon are good brands for instance.

1.2.4 Lighting Source

It is important for the wavelength of the light source to be very low (so as for it to be included inside the thickness of the oil film enough times and allow the interference phenomena to take place. The oil film thickness has an order of magnitude of microns) and for the light it spreads to be monochromatic and to be radiated through a diffuser (e.g.: semitransparent paper), so as to extend the lighting region. A low pressure sodium lamp, with a 589 nm wavelength, is highly suited for the OFI technique.

It is vital for the light source to be positioned with respect to the camera in a way such that it is feasible for it to visualize the fringes. This happens if the camera's lens can intercept the light rays reflected by the oil film. In CICLoPE this can be obtained by placing the light source and the camera

symmetrically with respect to the vertical axis of the pipe's section, using the two lateral accesses. In this way, the incidence angle of the light rays hitting the pattern will always be around 45 degrees. This also further points out the importance of spreading the light emitted by the lighting source.

1.3 The Procedure

1.3.1 Calibration

To evaluate the variation of fringe spacing across time in Oil Film Interferometry, photogrammetry is employed: two photographs of the interferometric pattern are taken at times t and t_0 . From each of them the mean spacing between the fringes is extracted. This evaluation is not trivial, there are different methodologies applicable to carry out the operation. However, this part does not constitute an element of difference between the two techniques discussed in chapters 1 and 2, except for the calibration step. To carry out the calibration, which in this case takes place before the test, it is necessary to acquire a picture of a piece of grid paper (divided into millimeters) attached where, during the run, the interferometric pattern will generate, with setup in position. In the picture caught, actually squared elements are deformed into rectangles. This knowledge allows for determining a geometric transformation able to restore the "real" dimensions of the image. Once the proportions have been modified in this sense, the calibration factor, given by the ratio between the length of a line in the image in millimeters and in pixels, is evaluated and the calibration step can be considered concluded.

1.3.2 Experimental Data Analysis

Evaluating the term $\Delta x/t$ means estimating the mean fringe spacing rate between two instants t e $t = 0$. In order to make the measurement more coherent with the real time evolution of the interferometric pattern throughout the run, during its course, it is possible to sample a series of pictures of the pattern in known instants, spaced by a preset time step, for instance 5 seconds. For each image evaluate the value of x and express it in a diagram as a function of the corresponding time instant. Then, interpolate the plotted points with a degree 1 polynomial, that is a straight line. Its angular coefficient will constitute the value of the mean fringe spacing rate $\Delta x/t$.

Just holding two samples of the spacing x , or, anyway, a reduced number of them, caught during the run, would make it feasible to obtain a discrete estimate of $\Delta x/t$.

The oil's viscosity, μ_{oil} , can be quantified by recording the mean temperature assessed in the experiment. Once this is acknowledged, it is possible, as a first alternative, to refer to the theoretical curve describing the evolution of the oil's viscosity as a function of temperature reported in the oil's manual and estimated by its producer. Otherwise, it is possible to produce a characteristic empirical curve of the oil, through experimental calibration with a viscosimeter. In this case, the viscosity will as well be expressed as a function of temperature.

For what concerns the term Δh_{oil} , thickness difference between two consecutive fringes, it can be attained via the following formula:

$$\Delta h_{oil} = \frac{\lambda_L}{2 \cdot \sqrt{n_{oil}^2 - n_{air}^2 \cdot \sin^2(\Omega_1)}} \quad (1.3)$$

, where λ_L is the wavelength of the light source, n_{oil} and n_{air} are the refractive indices of oil and air, while Ω_1 represents the incidence angle of the light rays which, once reflected by the oil and the surface, are captured by the camera. Ω_1 therefore contains the fundamental information of camera positioning. This makes it indispensable, in order for the procedure to yield results, to accurately know where the camera is positioned during the experiment. Moreover, it is compulsory to specify that such configuration must remain the same throughout the run or the photographs acquired would be associated to different incidence angle values.

It could be possible to implement the "reference technique" over tridimensional surfaces, but the interferometric pattern would look deformed in the pictures, due to the curvature of the surface on which the oil drop would be layed down, making the computation of mean fringe spacing uncertain. As a consequence, the results would not be very reliable. The "reference technique" may be adapted to the 3D case by exploiting the photogrammetry procedure described below for the alternative technique, but, even so, it would prove more expensive from a computational point of view, since it requires the evaluation of the mean fringe spacing x for a great number of images, e.g. 120, whereas the alternative technique only demands that this operation is carried out one time, namely for just one photograph.

$$\tau_w = \frac{\mu_{oil}}{\Delta h_{oil}} \frac{\Delta x}{t}$$

So, μ_{oil} becomes known from measuring the mean temperature during the experiment, is a constant simply obtained after Ω_1 gets fixed, $\Delta x/t$ is evaluated by measuring fringe spacing from each image acquired throughout the run. Once τ_w is known, the experiment is to be considered concluded. Then it is possible to to define the friction coefficient C_f as:

$$C_f = \frac{\tau_w}{\frac{1}{2}\rho_{air}u_b^2} \quad (1.4)$$

, where ρ_{air} is the mean density of air and u_b is the mean bulk velocity of the flow during the run. With this change, the results obtained may be compared with those deriving from other techniques and those that are present in the scientific literature.

2 Implementation of OFI over Arbitrary Surfaces

This "alternative" technique derives from the method proposed in Gluzman et al. (2022), in which a simplified photogrammetry procedure for an accurate measurement of wall shear stress over arbitrary geometries is described. As the authors of the technique state, when analyzing 3D surfaces through OFI, if model curvature is high, or the camera-to-model distance is short, uncertainties of the order of 10% in skin friction can be introduced as a result on an incorrect reading of the incidence angle. That's way photogrammetry becomes vital.

2.1 Theory

The technique is based on the mathematical formulation developed by Monson et al. (1993) for the assessment of superficial friction (C_f). Monson et al., in turn, gathered the starting considerations which led them to their own final expression from the work of Tanner and Blows (1976) about the deformation and thinning mode of an oil film immersed in an air flow. By the way, this points out that the equation does not depend on the nature of the duct in which the technique is applied, but only on the way in which the oil deforms when it undergoes the shear stress provoked by a flow in motion. The formula by Monson et al. was then reworked (and derived again, yet starting from the thin oil film equation) by Driver (2003) in the form also employed by Gluzman et al. (2022):

$$C_f = \frac{2n}{\lambda} \frac{\cos \theta_r \Delta x_f}{\int_{t_0}^{t_{run}} \frac{q_\infty(t)}{\mu(t)} dt} \quad (2.1)$$

In the expression, n is the refractive index of the oil, λ the wavelength of the employed lighting source, θ_r is the refraction angle of the light rays inside the oil, Δx_f the mean spacing of the interferometric fringes at the end of the experimental run, whose duration is t_{run} . The lower limit of integration t_0 , concerning the integral at the denominator, represents the instant in which oil starts to move and the interferometric fringes appear for the first time. It

would be necessary to take note of its, at least, approximate value during the run. $q_\infty(t)$ is the dynamic pressure in the freestream region of the flow, $\mu(t)$ the dynamic viscosity of the oil. Both the pressure and the dynamic viscosity are expressed as functions of time. This, because the formulation considers the chance that fluctuations of these variables might occur throughout the run.

The friction coefficient evaluated through this formula is defined as:

$$C_f = \frac{\tau_w}{\overline{q_\infty}} \quad (2.2)$$

, where $\overline{q_\infty}$ is the mean dynamic pressure recorded in the run.

Considering Snell's law and the fundamental relations of trigonometry, it can be noted that:

$$n \cos \theta_r = \sqrt{n^2 - n_{air}^2 \sin^2 \theta_i} \quad (2.3)$$

, where n_{air} is the refractive index of air, θ_i the incidence angle of the light rays hitting the test surface. It is possible to replace this expression in equation (2.1), obtaining:

$$C_f = \frac{2\sqrt{n^2 - n_{air}^2 \sin^2 \theta_i}}{\lambda} \frac{\Delta x_f}{\int_{t_0}^{t_{run}} \frac{q_\infty(t)}{\mu(t)} dt} \quad (2.4)$$

2.2 Experimental Setup

As regards the experimental setup of Gluzman et al.'s technique, test surface, oil, camera and light source undergo the same considerations being valid for the "reference technique". Once again, it is essential to remark that the light coming from the lighting source must be adequately diffused. (If one wanted to implement the method in the tunnel of the CICLoPE facility, the best positioning of the light source would probably be at the upper optical access of the pipe's test sections).

2.2.1 The Checkerboard

The checkerboard adds to the reference setup. It represents the tool through which the calibration step is carried out. Differently from the reference technique, this procedure does not involve a calibration prior to the experimentations, but it is necessary to carry it out again at each new run, evaluating once again the scale factor (or calibration factor). The pattern should be printed on an adhesive flexible and as much as possible thin piece of paper, in a way such that the checkerboard can conform to the hypothetical curvature of the surface over which it is applied. The checkerboard must be black and white, which an odd number of rows and an even number of columns. The tiles of the pattern must be all equal in size, square, and the length of their sides (in mm) must be known. The first column of the checkerboard is identified, in particular, because it shows a number of black squares greater than the white ones. These features are necessary so as for Matlab to recognize the pattern and assign the axes of the World Coordinates System.

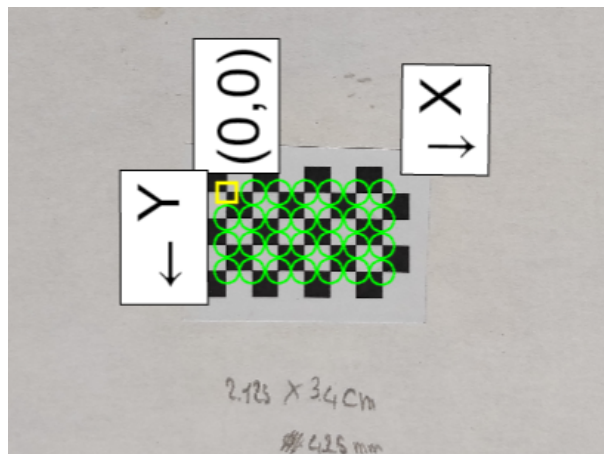


Figure 2.1: Checkerboard detecting and configuration of the world coordinates system (Camera Calibrator)

2.2.2 The Model

This procedure allows for the implementation of OFI over arbitrary geometries. A potential 3D test model is therefore to be added to the experimental setup. Gluzman et al. and before them Naughton et al. (2006) implemented OFI over "Gaussian bump" geometries (in addition to zero pressure gradient flat plates). As an alternative you might think of using an aerodynamic

profile or a different model surface of interest. The local curvature of the model's surface must not be excessive or Matlab's calibration tool may not work satisfactorily.

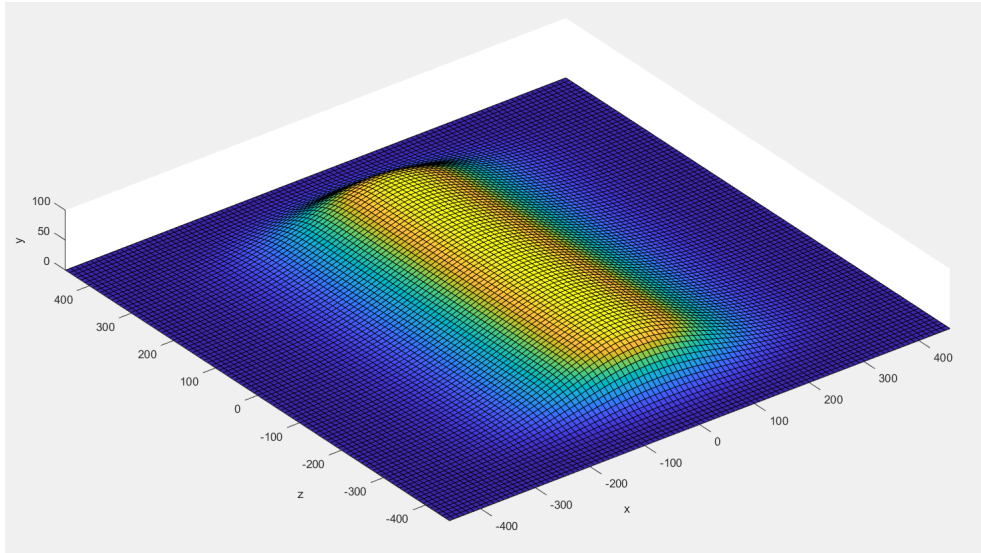


Figure 2.2: Gaussian bump geometry

2.2.3 Thermocouple and Dynamic pressure probe

These two instruments are necessary to record, through periodic sampling, the time evolution of temperature and dynamic pressure in the freestream, where they must be placed. The temperature information will then be converted in dynamic viscosity. Indeed, monitoring the oil's viscosity essentially means checking the development of temperature during the run, being viscosity a direct function of it. The available tools for passing from temperature to viscosity are the same discussed for the reference technique.

As an example, besides, Gluzman et al. report employing a K type thermocouple with a 10 Hz sampling rate.

2.3 The Procedure

Affix the checkerboard to the wall next to the glass over which the oil drop, main character of the experiment, is to be positioned. Deposit the drop onto the glass. Then, close the duct/the test section and start the flow. Record

the time instant at which the drop begins to deform, t_0 . The suggested run span is between 20 and 30 minutes. Once this time has passed, turn off the flow, open the duct and shoot a satisfactory number of photographs of the interferometric pattern and checkerboard placed side by side.

2.3.1 Experimental Data Analysis

With reference to equation (2.4), the evaluation of the term $\int_{t_0}^{t_{run}} \frac{q_\infty(t)}{\mu(t)} dt$ is carried out through the knowledge of the time history of dynamic pressure $q_\infty(t)$ in the freestream and oil's dynamic viscosity $\mu(t)$ during the run, obtained from the thermocouple and the dynamic pressure probe.

The terms which still are unknown in the equation are the incidence angle θ_i and the mean fringe spacing Δx_f . To estimate them, the camera calibration process has to be performed. Matlab, but it is not the only one program, offers an extension, which is part of the Camera Vision Toolbox, called "Camera Calibrator", which can be accessed via the application tab of the main desktop. The instrument is capable of acquiring a set of images fed in input to it and detect in each of them a recurring checkerboard pattern, whose real dimensions in millimeters are asked for to the user. Thanks to internal algorithms (least squares approximations...), the tool is able to evaluate all the camera's parameters. In particular, it assumes as valid a pinhole camera model:

$$w \begin{bmatrix} x_i \\ y_i \\ 1 \end{bmatrix} = \mathbf{K} [\mathbf{R} \quad \mathbf{t}] \begin{bmatrix} X \\ Y \\ Z \\ 1 \end{bmatrix} \quad (2.5)$$

, with separate addition of distortion effects. The calibration tool simultaneously evaluates the camera's intrinsic matrix \mathbf{K} , the extrinsic parameters, different for each image received in input (and defining the position of the pattern with respect to the camera and vice versa), that is \mathbf{R} , 3D rotation matrix from camera to world coordinates system, and \mathbf{t} , translation vector from camera to world coordinates system, and the distortion coefficients, which can be divided in radial and tangential (the estimation of radial coefficients is usually sufficient for a good "undistortion"). w is the scale factor and the calibration tool does not give an estimate of it.

The technique here described involves applying a checkerboard next to the small plate over which the oil film will warp during the run. In this way it will be possible to exploit the results of the calibration step.

The fundamental assumption the algorithm makes is that the checkerboard, in each of the images received, is completely flat, independently of the fact that the surface over which it is applied does or does not display a tridimensional geometry. The intrinsic parameters, through \mathbf{K} , and the distortion ones, estimated with the Camera Calibrator are then such that, performing a distortion removal operation from the single images, these will a posteriori present a flattened checkerboard. The algorithm basically attributes all the blame for the checkerboard's distortion to the camera, ignoring the possibility that the test surface could have a geometry different from the flat one. It is possible to exploit this aspect for attaining pictures of the interferometric pattern that are not affected from the tridimensionality of the studied surface.

The described instrument requires as input a minimum number of checkerboard images of 2; providing at least 3 of them, as Gluzman et al. (2022) do, is nevertheless recommendable. The more images are employed, the more the calibration algorithm will manage to yield precise results. The images should better be captured from sufficiently different positions and angles, but it is not strictly necessary for everyone of them to clearly display the interferometric pattern; however the checkerboard should be distinctly identifiable. Just the picture to be used for computing Δx_f and the scale factor must plainly show the pattern. Considering the importance of this image, it is suggested to acquire it with a low incidence angle, since the assessment of the distances proves to be more accurate if it involves more pixels and this happens with a smaller incidence angle. For further precision, it is to be noted that the pattern image does not allow for a direct evaluation of Δx_f , but, instead, a length $\Delta x_{f,image}$ is first measured, which should then be projected onto the x-y plane of the world coordinate system via multiplication with the scale factor, obtaining the actual value for Δx_f . An evaluation of the scale factor along the greater dimension of the checkerboard is therefore needed, once the image has had its distortion effects removed. To do this, it may be viable to average the horizontal distance (in pixels) between the adjacent points of the checkerboard and then divide the actual modulus of a tile's side, expressed in millimeters, by this mean. As a way to reduce the error of this calculation, once again, it may be recommendable to take the pictures

with a low incidence angle, since the bigger the incidence angle, the more the real proportions of the elements of the checkerboard will be distorted due to the differentiated distance of its points from the camera's optical centre, i.e. the point to which all the light rays captured by the device converge (as common experience proves, farther objects look smaller), resulting in a lower number of pixels involved in the average. It may as well be possible to express the distancing between the checkerboard's corners and, accordingly, the scale factor as a function of position in the image, making the algorithm more precise the evaluation of the fringe spacing rate.

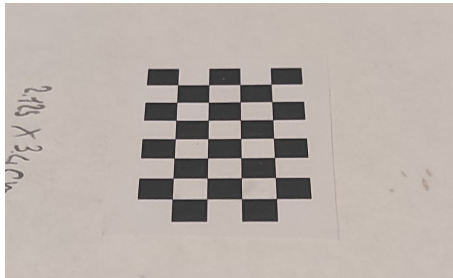


Figure 2.3 : The farther tiles look shorter along the horizontal direction (in image coordinates the vertical direction)

As the scale factor ($\frac{metri}{pixel}$) has been determined, the mean distancing between fringes is left to be computed. To do that, different ways can be chosen, though not constituting dissimilarity between the reference and alternative technique, as mentioned before. Thereafter, $\Delta x_{f,image}$, in pixels, is first found, then Δx_f , by means of the scale factor.

Finally, it is necessary to have an assessment of the incidence angle θ_i , which, due to the law of reflection, can be considered equal to the reflection angle, namely the angle included between the direction orthogonal to the checkerboard's plane and the central point of the interrogation area extracted from the image and used for the computation of $\Delta x_{f,image}$. The position of the camera is indeed known, through the extrinsic parameters obtained from the calibration phase, and can be employed for this purpose.

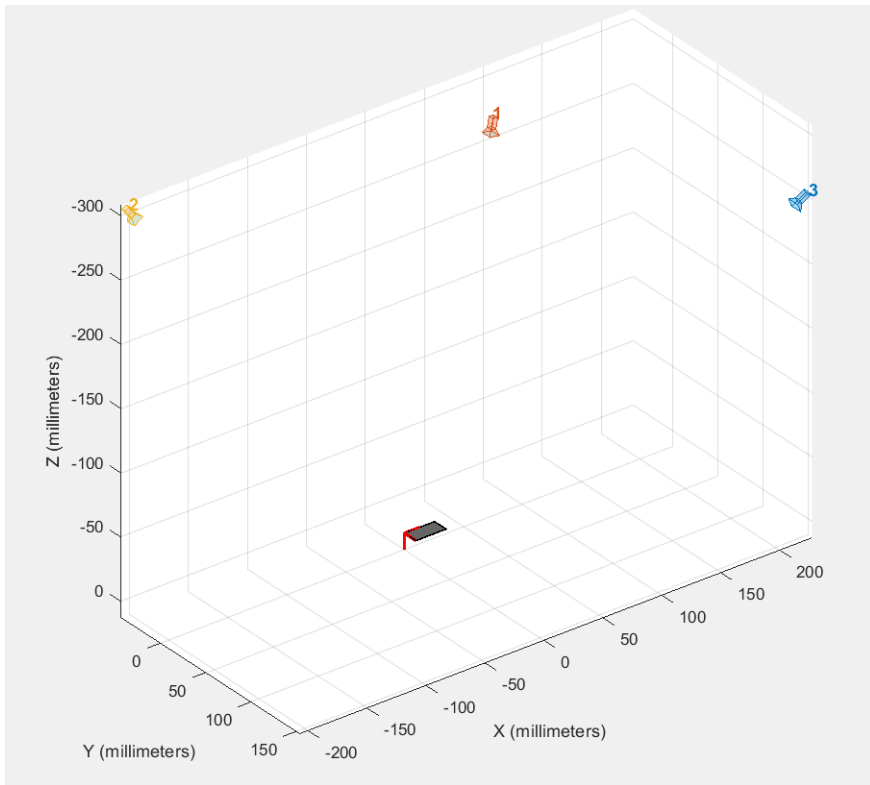


Figure 2.4: Visualisation of the extrinsic parameters (World Coordinate System)

Once all the terms of equation (2.4) are known, the friction coefficient Cf can be computed.

3 Test Case and Validation

3.1 Theoretical Results

A comparison of the two discussed methodologies is now reported, pointing out their benefits and drawbacks.

Both techniques prove to be strongly influenced by a correct evaluation of the oil's viscosity. It is therefore very important for it to be correctly estimated and for the thermocouple used to yield accurate measures.

The reference technique is robust. Possible discontinuities in the deformation rate of the oil film have little influence on the overall spacing rate value if the number of samples acquired during the run, that is photographs, is made large, as in this method. Moreover, thanks to the nature of the technique, it is possible to exclude from the measurement the tunnel's transients, start up and shut off respectively. Non constant tunnel running conditions as transients can, as a matter of fact, constitute an error source, as they generate working conditions different from the one desired for the particular test carried out (the condition of flow at regime).

This technique require the experimental setup to be accurately arranged, since this affects the final computation via Δh_{oil} . Its positioning must not be modified during the test. The strict disposition required from this setup would make it tough and time consuming to carry out OFI measurements at different points of a surface. At least without modifying the technique by implementing photogrammetry expedients, each time it would be necessary to move the entire setup, or, if possible, the geometry, so as for it to always be in the same relative position with respect to the instruments. Furthersome, in case photogrammetry was not applied, once again, it would not be possible to carry out simultaneous measures at different points in the same run. The alternative technique is more flexible in this sense and grants more freedom. It only involves shooting the photographs once the run has ended and the tunnel has been opened. Indeed, the mathematical formulation employed by this technique, equation (2.4), only asks for the final value Δx_f of the fringe spacing. Just having to elaborate one photograph, the complexity of computation and data acquirement is kept restrained. Besides, a priori knowledge of the position and angular orientation of the elements, with particular regard for the camera, is not required, as long as the interferometric pattern is well discernable (as enlightened by the monochromatic light source). This

advantage makes it possible to reduce the time and efforts needed for setup preparation and allows for carrying out measurements in different points of the tested surface, that may as well be simultaneous.

It must be restated that, differently from the reference method, makes it feasible to measure aerodynamic skin friction over tridimensional not a priori known surfaces.

Nevertheless, the alternative technique employs runs of an around 20 minutes span, whereas the reference one only asks for 10 (or less). The reason for this comes from the necessity of minimising the uncertainty determined on the final result by the start up and shut off transients, which are included in the test by the alternative technique. Indeed, as claimed by Driver (2003), it is reasonable, retaining a certain level of conservativity, to assume such uncertainty to be proportional to the ratio between the time employed by the start up and shut off transients and the overall time duration of the run. Gluzman et al. (2022) suggest the resulting uncertainty over C_f , for a total 40 seconds span employed by the transients, to be around 0.7 %, overestimated. Driver (2003) underlines that the uncertainty related to the transients would be cut off if it was possible to acquire two images spaced in time during the run (as the reference technique implies). Indeed, formula (2.1) was born to be applied to wind tunnels with no optical access, accessing the duct only once the run is over. However, nothing forbids modifying it as follows:

$$C_f = \frac{2n \cos \theta_r}{\lambda} \frac{(t_2 - t_1)}{\int_{t_1}^{t_2} \frac{q_\infty(t)}{\mu(t)} dt} \frac{\Delta x_f}{t_2 - t_1} \quad (3.1)$$

, where t_1 and t_2 would be the two instants at which the pictures mentioned by Driver would be taken (they must be chosen away from the transients) and Δx_f the mean fringe spacing variation recorded in the time interval enclosed by them. This formula is analogous to equation (1.2), but a little more accurate since it considers the time evolution of dynamic pressure and oil's viscosity throughout the experiment. It is also possible to average the value of $\Delta x_f/(t_2 - t_1)$ over the time interval analysed, as done for the reference technique by sampling a series of images between time instants t_1 and t_2 . Clearly, this change can only be implemented in case the tunnel used for the test is equipped with optical accesses.

3.2 Data Presentation

Some OFI measurements were carried out on a flat SF11 glass surface at the CICLoPE wind tunnel facility in march/april 2023. This section of the thesis will be dedicated to the exposure of the algorithm employed for elaborating the data gathered from these experiments. The tested duct is endowed with a series of optical accesses placed at different test sections on its long pipe. Each test section accounts for four optical accesses, one at the top, one the bottom and two lateral ones. On the section's circumference, they are spaced by 90 degrees angles. Equation (3.1) was therefore used and some results were derived.

The following is a list of the features of the experiments performed:

- The experimental setup used is mainly the one described in chapter 1, in particular with a nominal value of 45 degrees for the incidence angle Ω_1 , since the tunnel's lateral accesses were employed;
- Unfortunately, no test model was used and OFI was only implemented on a flat surface with the aim of observing the variation of skin friction as the Reynolds number changed;
- Seven experiments, distinguished by different RPM numbers of the facility's fan, going from 200 to 500 with step 50, were carried out;
- Two thermocouples were switched on during the tests, one positioned in the freestream and one attached to the wall, which allowed for determining the oil's viscosity's development throughout the tests;
- The pitot tube present in the freestream was unfortunately turned off, but the static pressure ports positioned along the pipe's length were reading correctly. This allowed for having an estimate of skin friction via the pressure drops method as well and also an evaluation of the bulk velocity of the flow in the tunnel, which was recorded as a time average over the entire duration of the runs. It was used for attaining the value of the dynamic pressure $q_\infty(t)$, coupled with approximated values of the air density ρ_{air} , drawn from similar experiments conducted at analogous RPM numbers.

Each of the experiments (runs) conducted produced the following outputs:

- A folder named after the number of RPM at which the tunnel was operating, containing 120 pictures of an oil film obtained using a 50 cSt Clearco Dow Corning 200 oil. The pictures were sampled with a Nikon D5600 digital camera, with a resolution of 4496x3000 pixels and a time delay between the instants of acquirement of consecutive photographs of 5 seconds. An 180 mm lens was used. The first and last images were captured sufficiently away from the ignition and shut off transients, respectively, for a total of 600 seconds considered, that is 10 minutes. All the pictures were caught with the same position of the camera, namely at a nominal value of 45 degrees incidence angle (in practice, the angle was a little different);
- A temperature .txt file containing as 2 columns the readings of the two thermocouples above mentioned, caught with a 20 Hz sampling rate for the 10 minutes relative to the collection of the pictures, that correspond to roughly 12000 rows (evaluated instants);
- A .mat file named "Flow-quantity", containing the information of the mean bulk velocity in the tunnel in each of the experiments carried out and deriving from the samplings relative to the pressure drops method, which was carried out simultaneously.

3.3 The Procedure

This section contains the description of the procedure set up for elaborating the available data. The will was to produce a generalized algorithm capable of processing OFI data obtained from tests on any arbitrary tridimensional geometries, despite only managing to employ it for a flat geometry in this case.

The used procedure is a combination of the two described in chapters 1 and 2, joining the parts of them best suited for attaining accurate results and suitability relatively to a practical application of OFI in the CICLoPE wind tunnel facility, where the data above listed were collected.

Another purpose was also to obtain an estimate of skin friction not just at a single point of a surface, but to use the same interferometric patterns for obtaining an estimate of the evolution of Cf as a function of position along the length of the interrogation area extracted from the interferometric patterns themselves. Then, to observe whether the difference between distinct

points would or would not be appreciable.

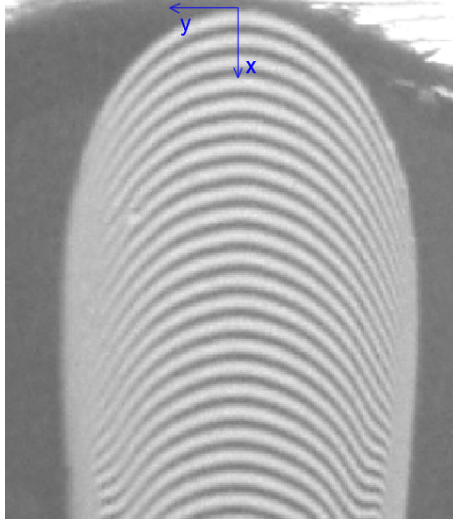


Figure 3.1: Example of an interferometric pattern

Unfortunately, that appraisal was not fully viable, having the experiments been conducted on a flat surface. Anyway, the algorithm still carries out the computation, along with the evaluation, as functions analogous to the one for Cf , of these other quantities: the scale factor, a variable expressed in $\frac{mm}{pixels}$ which makes it possible to convert pixel scales in real distances via multiplication; the incidence angle θ_i , which can be derived thanks to the information deriving from the camera calibration session, with no need for prior knowledge of camera position.

3.3.1 Camera Calibration

This step is derived from Gluzman et al.'s technique and is fundamental for determining the camera parameters relative to the studied test. The pictures gathered in the case study defined by the list in subsection 3.2 do not contain any calibration checkerboard, as the pictures were taught to be used for a "traditional" implementation of OFI. That is, the original calibration step was carried using a piece of grid paper (divided into millimeters), which was attached to the SF11 glass test surface. The tunnel was closed, the Nikon camera and the rest of the setup were put in place and a picture was taken, with the same zoom level intended to be used for the successive experiments.

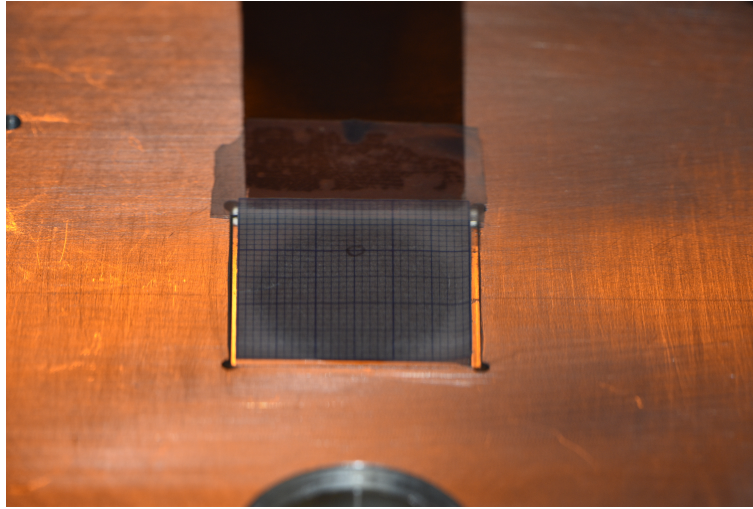


Figure 3.2: Image of the calibration grid paper, with enhanced brightness.
3x3cm grid paper

Considering the distortion which the calibration pattern's sides are subjected, a trial was made to join a suitable size checkerboard, in pixels, to one of the images gathered: the central 1x1cm square in the image above has an aspect ratio of around 1.455 (width/height) and the scale factor along the horizontal dimension of the image, parallel to the direction of deformation, is around 0.0219 mm/pixel. These informations were used for attaching a 2.25 mm square's size checkerboard to the one picture mentioned above, gaining the following:

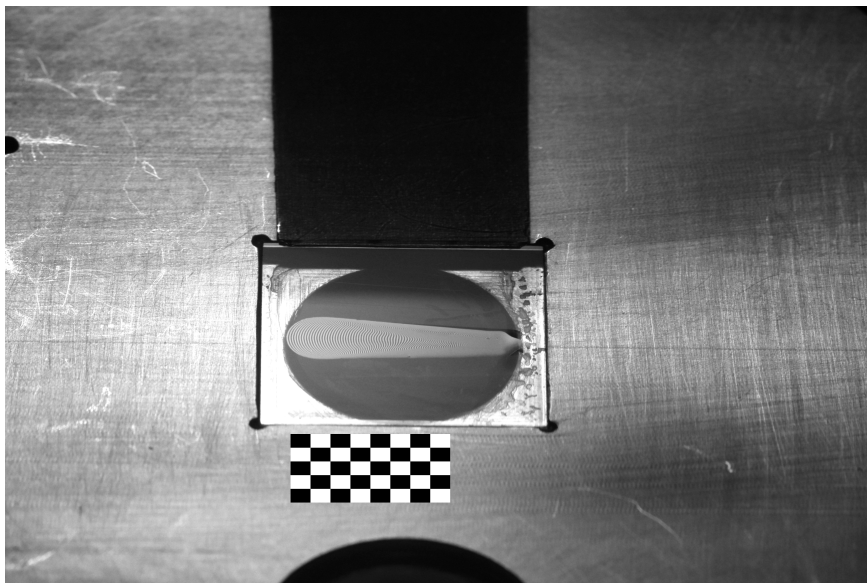


Figure 3.3: Joined pattern and checkerboard

A geometrical affine transformation was then searched for in order to acquire an image in which the checkerboard would not be distorted, equivalent to an hypothetical photograph shot from directly above the pattern. This achievement would be necessary in order to have enough images to then feed to the camera calibrator. Indeed the calibrator's algorithm requires at least 2 images, equal in size, captured from different camera locations and angles and containing a checkerboard. The following image was therefore attained:

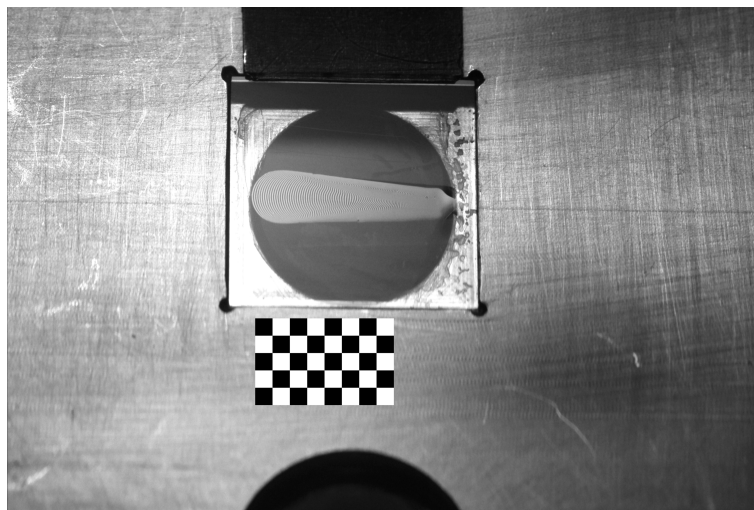


Figure 3.4: Picture containing the "real" size checkerboard

More images originated from this could then be derived, by using Matlab's "Camera Toolbar" commands, displayable by opening the "View" tab in the figure space.

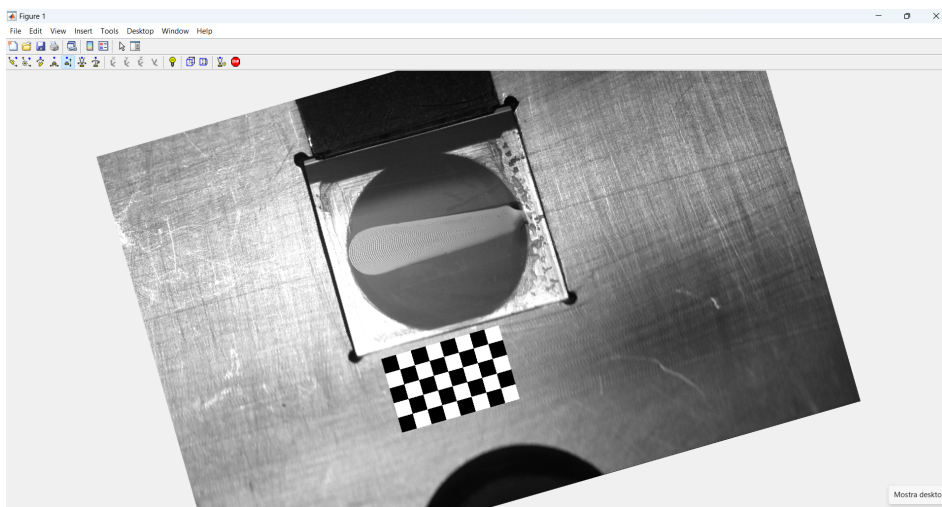


Figure 3.5: Camera displacement using Matlab's camera calibration toolbar

The images obtained, which at this point could have potentially been infinite, were fed to Matlab's Camera Calibrator so as to try and deduce the camera parameters.

Unfortunately, the tool was not able to perform a correct calibration and the results yielded for the synthetically produced images were unsatisfactory.

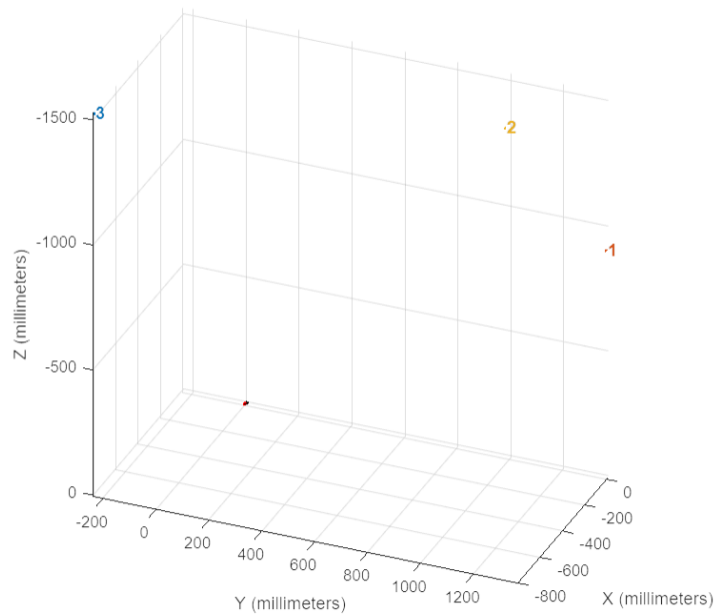


Figure 3.6: Example of an unsuccessful camera calibration session resulting from the images in figures 3.3, 3.4 and 3.5

As can be seen, in this case the position of the camera is not well recovered for all pictures. E.g. camera position 2 clearly does not match figure 3.4, in which the checkerboard pattern possesses "actual" proportions, meaning the camera should result positioned directly above the pattern.

This may be due to the fact that the checkerboards employed were artificially generated, meaning their square tiles had perfectly straight sides, whereas the algorithm expects some deformation from them.

Indeed, trials performed using pictures obtained from real models output correct results.

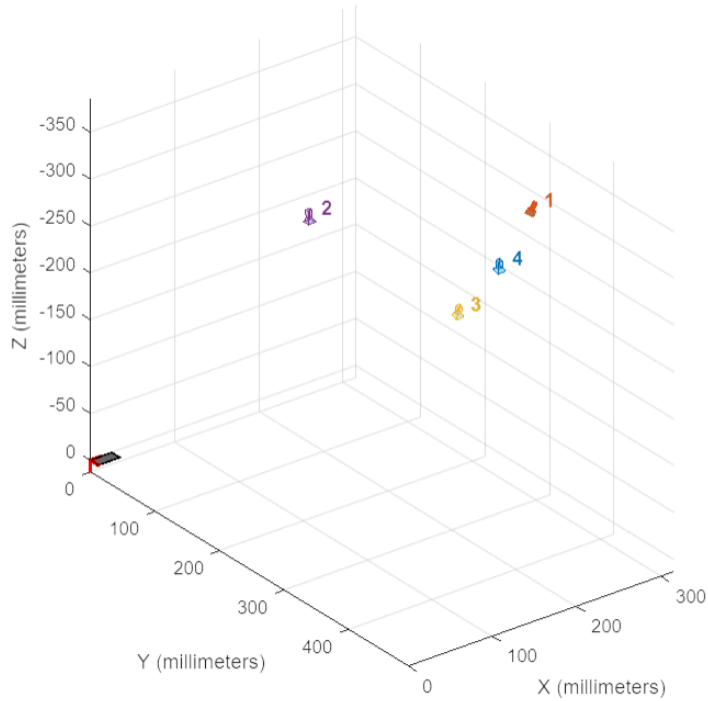


Figure 3.7: Example of a successful camera calibration session (pattern centric view, 4.25mm tiles)

Another aspect to consider when going through this step is that the Camera Calibrator does not understand the concept of zooming. Calibration trials performed using only zoomed images, with the same degree of magnification, yielded improbable extrinsic parameters: the locations determined for the camera in the different cases did not give a reliable reading of the depth of the image, in spite of quite well deducing the camera's position in terms of x and y world coordinates.

This constitutes quite a problem if the will is to apply OFI to a large wind tunnel acquiring pictures through its optical accesses. Zooming becomes almost imperative for achieving high resolution pictures of the interferometric patterns, essential for a good evaluation of fringe spacing distance.

In OFI applications, the Camera Calibrator tool basically needs to fulfill two purposes:

- be capable of recovering the original position of the camera in the provided pictures, so as to then use this information for precisely computing the incidence angle with respect to the interferometric pattern;

- derive the camera parameters necessary for performing a distortion removal operation on warped (due to surface curvature) pictures of interferometric patterns.

As mentioned, zoomed in images cannot be used for estimating the correct position of the camera, but the camera parameters derived by using them consent a qualitatively satisfying distortion removal operation from the pictures of the interferometric patterns. On the other hand, photos which have been obtained using the standard focal length of the camera, that is no zooming essentially, allow for precisely determining camera position in a range of 20/50cm of distance from the checkerboard, but if the pictures are taken from too far away, "image undistortion" via the estimated camera parameters performs poorly, as happens, by the way, when camera-to-model distance is too short; moreover, in this case, it appears that the algorithm is only capable of recovering the correct relative angular position dividing camera and checkerboard, but not to give an accurate estimate of the depth of the images. This would actually be sufficient for OFI's purposes, since it makes it possible to compute the incidence angle.

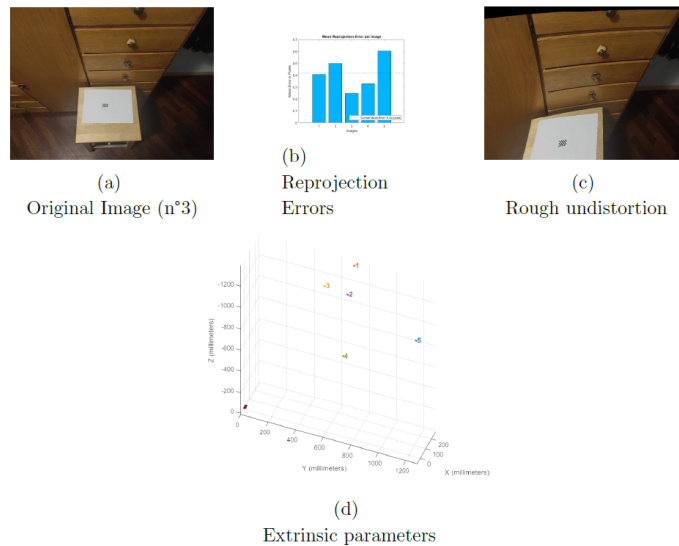


Figure 3.8: Example of a camera calibration session performed with pictures taken at a great distance from the checkerboard (position number 3 is represented by the yellow dot)

In the previous figures, it can be noticed that, regardless of the camera's depth wrong reading (figure (d)), which causes an unsatisfactory distortion removal, as figure (c) displays, the angle between the camera and the checkerboard is correctly recovered. The mean reprojection errors, figure (d), are the mean distances between the points of the checkerboard detected in the original image and the reprojected points, whose location is found by the algorithm via undistortion application. In the case of implementation over a flat geometry, the closer they are to zero, the smaller is the magnitude of the employed camera's distortion effects.

The idea for implementing the technique in a large pipe such as CICLoPE, also taking advantage of its optical accesses, may then be to perform a "double" camera calibration: before the run, take at least two pictures of the checkerboard from different positions and view angles, then place the camera in the exact location where it will stand during the run and take another picture with the same degree of zoom, which I suggest addressing as first. Use these photographs for carrying out a camera calibration session, through whose results computing θ_i at a later time. During the run, acquire zoomed pictures of the interferometric pattern plus checkerboard set, but be careful not to zoom in too much. The focal length chosen should be such that the picture taken resembles a picture taken from a distance between 20 and 40/50cm, as mentioned. This way you will be able to retain precision in computing fringe distancing, then, once the run has ended, open the tunnel and take at least two other pictures of the checkerboard from different camera positions, but employing the same focal length (zoom level). The second calibration session deriving from these pictures will yield the camera parameters necessary for performing the fringe region distortion removal operation. All the efforts listed above have the aim of enabling the implementation of OFI over 3D surfaces in a large wind tunnel with available optical accesses and retaining the maximum feasible precision.

Unfortunately, the data held in this case, did not undergo such treatment and it was not possible to verify the full correctness of the propositions here listed. Therefore and besides, the corresponding OFI results were to be attained considering the "nominal" incidence angle of the camera, 45 degrees, whose reliability depends on the precision of the tripod used for holding it in place.

3.3.2 Image Processing and Calculations

This subsection describes the processing the images gathered have to undergo for extrapolating data from them.

First of all, the 120 4496×3000 resolution images, which by default were stored in order in the same folder, had to be read in a Matlab $4496 \times 3000 \times 120$ third order tensor "IM". Before doing that, the pictures, which themselves are third order tensors, as *RGB* images (which are treated as *width x height x 3* tensors, being their three dimensions the storages of the red, green and blue saturation values of each pixel), have to be converted to second order tensors and, consistently with OFI purposes, that is here done by considering the brightness of every single pixel. That is achieved by first transforming each *RGB* image in a *HSV* (hue, saturation, value, namely brightness, image) picture, using Matlab's `rgb2hsv` function, and drawing from it the third second order tensor component, which stores the brightness of the pixels itself. This can also be done by converting the *RGB* images to black and white images using Matlab's `rgb2gray` function.

Once the brightness matrices have been extracted, image undistortion has to be performed by using the camera's parameters attained from the calibration step. In the analyzed case, image undistortion actually introduced an error, since it was carried out using synthetically produced images.

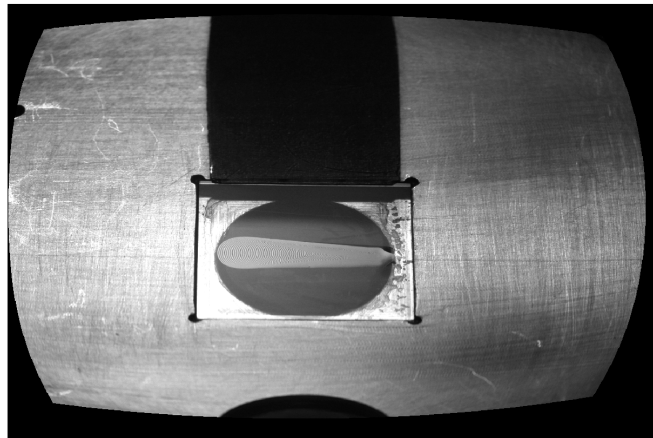


Figure 3.9: Distortion removal (incorrect) on a fringe pattern

After image undistortion, which, it is to be remembered, serves as a way of annihilating fringe distortion caused by the 3D surface's curvature, the images have to be rotated of a certain angle in a way such that the interferometric pattern gets perfectly vertical. This is necessary for allowing the cropping of the "Interrogation Area", namely the region of the fringe patterns that is to be used for computing the fringe spacing rate. This particular angle can be computed by using the checkerboard's sides, thanks to the fact the camera calibration step also yields the precise position of the checkerboard's corners in the undistorted image in a variable called "ReprojectedPoints".

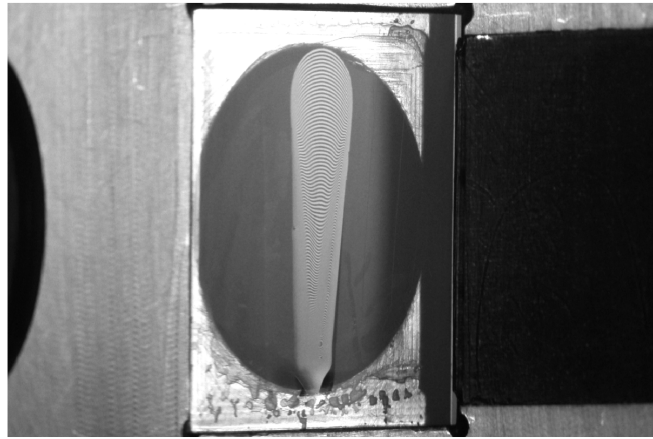


Figure 3.10: Rotated interferometric pattern

At this point, the pictures stored in the IM matrix, which have been updated with the new rotated, then undistorted images have to be cropped. A selection of the interrogation area step is therefore performed. The user is asked for cropping the interrogation area as a rectangular region in the first, and most fringe dense, image among the ones contained in IM.

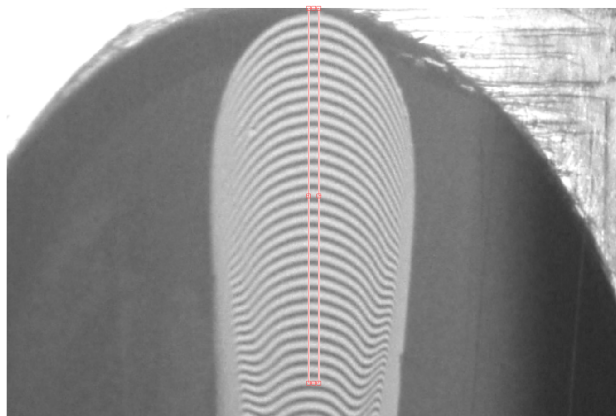


Figure 3.11: Selection of the interrogation area

When the interrogation area's boundaries have been defined, all images contained in the matrix IM are cropped the same way, obtaining a smaller "int-areas" third order tensor.



Figure 3.12: Interrogation area

The images contained in "int-areas" are then averaged along their rows obtaining a second order tensor "light-signals", having a number of rows equal to the height of the interrogation area and a number of columns of 120, namely the number of photos processed. The "light-signals" matrix is fed to a function "spacing-rate", which uses it for computing the spacing velocity of the fringes, knowing the photos were shot every 5 seconds:

- fringe spacing in pixels is first computed between all the fringes detected in the interrogation area;
- then, its values are ascribed to the pixels representing the average position between the peaks of the signals, which constitute the center of the white fringes and whose distance is the computed fringe spacing itself;
- the discrete points found, expressible as (pixel coordinate of the mean point between consecutive peaks, fringe spacing), are thus joined with straight lines and the resulting interpolating function is evaluated in all pixels of the interrogation area;
- the spacing vector obtained is multiplied times the scale factor vector previously evaluated along the interrogation area, in order to convert the spacing from pixels to millimeters, and saved in a column of a matrix one may call "mm-spacing".

These passages are repeated for all 120 light signals. Thus, a time vector "t", containing the time instants at which the pics were acquired (in increasing order), is created and used for interpolating all rows of the matrix "mm-spacing", representing the discrete values of the spacing at the instants contained in t, with a degree 1 polynomial, that is a straight line. The slope of these curves will constitute the values of the fringe spacing rate at each pixel of the interrogation area.

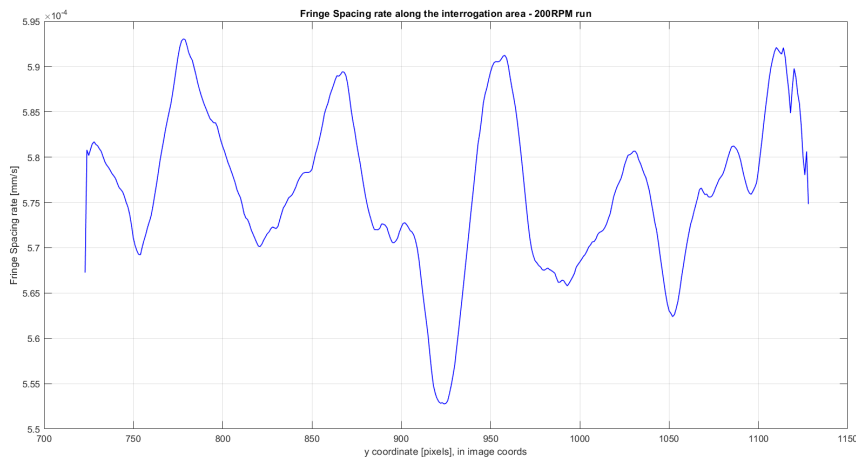


Figure 3.12: Fringe spacing rate along the interrogation area

Once the spacing rate $\frac{\Delta x_f}{t_2 - t_1}$ is computed, the only things left are estimating the incidence angle, as a function of position along the interrogation area (which actually is not so mandatory, being that the incidence angle actually does not change so much along the fringe pattern: Gluzman et al. themselves suggest the incidence angle varies below 0.2° in the selected rectangle of interest), which in this case, as discussed, was not assessable, and evaluating the integral at the denominator of equation (3.1), that is the mean ratio throughout the run between the dynamic pressure $q_\infty(t)$ in the free stream and the dynamic viscosity of the oil μ_t .

Luckily, temperature was sampled during these runs and stored in .txt files: the temperature readings by the two thermocouples used are therefore averaged and expressed as a function of time during the run. 50 cSt oil was used for the tests, with a (assumed) refractive index $n = 1.4024$ and a (assumed) nominal density $\rho = 964 \text{ kg/m}^3$ at 25°C , for which the viscosity-to-temperature law provided by the oil's producer was employed. A Clearco oil was used. Gluzman et al. (2022) report Clearco oils' viscosity-to-temperature law, which was thus used for this thesis as well:

$$\mu(T(t)) = \rho 10^{(-6 + \frac{763.1}{273.16 + T} - 2.559 + \log(\nu_0))} \quad (3.2)$$

, where T is the temperature, expressed in $^\circ \text{C}$, ρ and ν_0 are the oil's nominal density and kinematic viscosity at 25°C , expressed in kg/m^3 and cSt respectively (log is the 10 base logarithm).

On the other hand, dynamic pressure was not gathered and the only way for evaluating it was to assume a likely value for the air's density, on the basis of available data obtained during runs at analogous RPM numbers, and to exploit the results for the flow's mean bulk velocity in the tunnel during the run deriving from pressure drops (namely, from static pressure ports along the pipe) measurements, which were simultaneously carried out.

$$q_\infty(t) = \frac{1}{2} \rho_{air}(t) u_b^2 \quad (3.3)$$

4 Results

At these point, all the outcomes collected were joined through equation (3.1), obtaining an evaluation of Cf as a function of position along the interrogation area.

$$C_f = \frac{2\sqrt{n^2 - n_{air}^2 \sin^2 \theta_i}}{\lambda} \frac{(t_2 - t_1)}{\int_{t_1}^{t_2} \frac{q_\infty(t)}{\mu(t)} dt} \frac{\Delta x_f}{t_2 - t_1} \quad (4.1)$$

Cf was then also averaged, gaining a mean value of skin friction on the area tested. By simply disregarding the $q_\infty(t)$ term at the denominator of equation (4), it is possible to obtain the formula for aerodynamic friction/tangential stress τ_w .

As usually defined for a pipe duct, the bulk Reynolds number was computed using the tunnel's radius R :

$$Re_{bulk} = \frac{\rho_{air} u_{bulk} R}{\mu_{air}} \quad (4.2)$$

And the friction Reynolds number was consequently evaluated as:

$$Re_\tau = \frac{\rho_{air} u_\tau R}{\mu_{air}} \quad (4.3)$$

, where u_τ represents the friction velocity, which can easily be found once τ_w is known, as:

$$u_\tau = \sqrt{\frac{\tau_w}{\rho_{air}}} \quad (4.4)$$

Hence, the following results were output for the data analyzed:

Overall Results						
RPM	Re_{bulk}	C_f	$\tau_w [N/m^2]$	$u_\tau [m/s]$	Re_τ	$Sp.rate [\mu m/s]$
200	233500	0.003381	0.12812	0.3244	9730	0.5764
250	295500	0.003269	0.19830	0.4037	12110	0.8923
300	359000	0.003121	0.27921	0.4792	14380	1.2622
350	422000	0.002941	0.36366	0.5471	16410	1.6527
400	486500	0.002769	0.45174	0.6116	18350	2.1270
450	550500	0.002538	0.53037	0.6627	19880	2.4972
500	614000	0.002522	0.65601	0.7370	22110	3.0888

RPM	$Oil [cSt]$	$\mu_{oil} [kg/ms]$	$q_{mean} [Pa]$	$\rho_{air} [kg/m^3]$
200	50	0.05413	37.89	1.217
250	50	0.05405	60.67	1.217
300	50	0.05380	89.46	1.216
350	50	0.05352	123.65	1.215
400	50	0.05165	163.16	1.208
450	50	0.05165	209.00	1.208
500	50	0.05165	260.14	1.208

In the table above, the Reynolds number Re_{bulk} readings from pressure drops were rounded to the closest multiple of 500. The friction Reynolds number Re_τ was rounded to the closest multiple of 10 instead.

It is to be remarked that all the values obtained from "optical data", namely photographs essentially, e.g. the spacing rate, C_f itself and τ_w , strictly depend on a correct evaluation of the calibration factor, which, for the conclusions reached in subsection 3.3.1, had to be manually performed.

Below are the C_f results previously obtained for the same tests via an old algorithm used for OFI measurements which employs oil's viscosity calibration curves, and the pressure drops method, respectively. The flow's mean bulk velocity readings throughout the runs are also reported:

RPM	$C_{f ofi}$	$C_{f dp/dx}$	$u_{bulk}[m/s]$
200	0.003235	0.003337	7.89
250	0.003135	0.003181	9.99
300	0.003076	0.003064	12.13
350	0.003091	0.002971	14.27
400	0.002887	0.002884	16.44
450	0.002723	0.002822	18.60
500	0.002705	0.002769	20.76

The results gathered were then plotted together with some approved logarithmic skin friction laws and more recent empirical curves from McKeon et al. (2005), which are included below.

In these equations, the bulk Reynolds number Re_b was defined using the pipe's diameter and, for a successive comparison, this was to be considered. The term λ is called friction factor and can be obtained through C_f as:

$$\lambda = 4C_f = 8 \left(\frac{u_\tau}{u_b} \right)^2 \quad (4.5)$$

Prandtl-von Kármán logarithmic friction relation:

$$\sqrt{\frac{1}{\lambda}} = 2 \log \left(Re_b \sqrt{\lambda} \right) - 0.8 \quad (4.6)$$

Equation (3.1) by McKeon et al.:

$$\sqrt{\frac{1}{\lambda}} = 1.930 \log \left(Re_b \sqrt{\lambda} \right) - 0.537 \quad (4.7)$$

, based on pipe friction data from the Superpipe facility and predicting the pipe's friction for Reynolds number range $31 \times 10^4 \leq Re_b \leq 18 \times 10^6$

Equation (3.5) by McKeon et al.:

$$\sqrt{\frac{1}{\lambda}} = 1.920 \log \left(Re_b \sqrt{\lambda} \right) - 0.475 - \frac{7.04}{\left(Re_b \sqrt{\lambda} \right)^{0.55}} \quad (4.8)$$

, which also corrects for the deviation of the experimental data from the logarithmic friction law due to the viscous effects. The pipe wall friction data from CICLoPE used in Zanoun et al. (2021) were reported to show agreement with equation (4.8) within $\pm 0.5\%$ for $13 \times 10^4 \leq Re_b \leq 2 \times 10^6$.

These literary data are reported and thoroughly examined in the cited document.

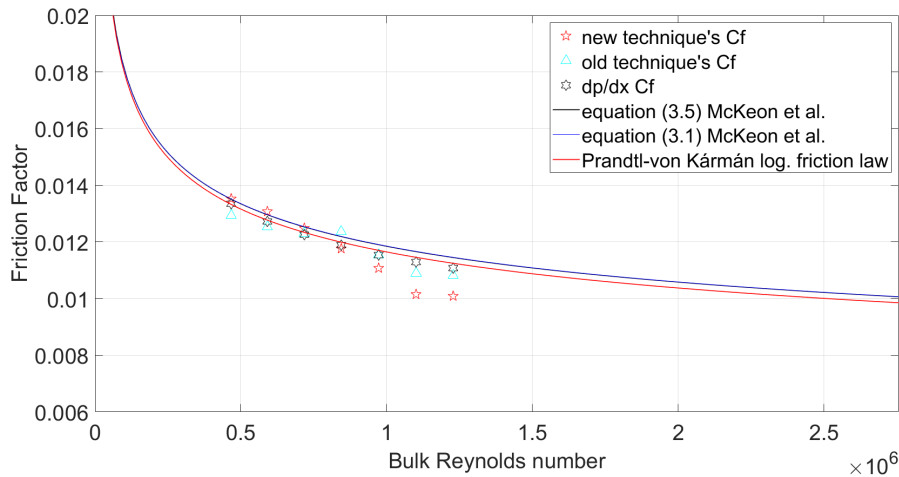


Figure 4.1: Final friction results

As expected, the newly obtained results do not fully show large agreement with the curves drawn from scientific literature. Indeed, the pictures of the interferometric patterns were corrected using unlikely camera parameters got from unsuccessful camera calibration sessions, carried out using synthetic images. Besides, no oil calibration curves were used, in contrast to old OFI measurements. The gap between the theoretical curves and the attained experimental, in particular, seems to get more consistent with higher Re_{bulk} values.

However, the main behaviour of the friction factor for increasing Reynolds number is the one it should have, that is skin friction decreases as the bulk Reynolds gets larger.

The results from the pressure drops method are, in this case, the ones which overall display better agreement with the known curves and especially with the Prandtl-von Kármán logarithmic friction relation. Anyway, it is to be noted that, for the three first values of Re_{bulk} , the newly OFI obtained results are the closest to McKeon et al.'s empirical curves.

Another aspect which may be observed is the fact that, as the Reynolds increases and in particular, for the three last positions, the diverging behaviour, with respect to the black and blue curves, of the cyan and red dots seems to be analogous, even though more emphasized for the new results. This may be due to issues in the evolution of the interferometric oil patterns caused by

dirt present in the flow, since the facility's refiners were temporarily removed for maintenance purposes.

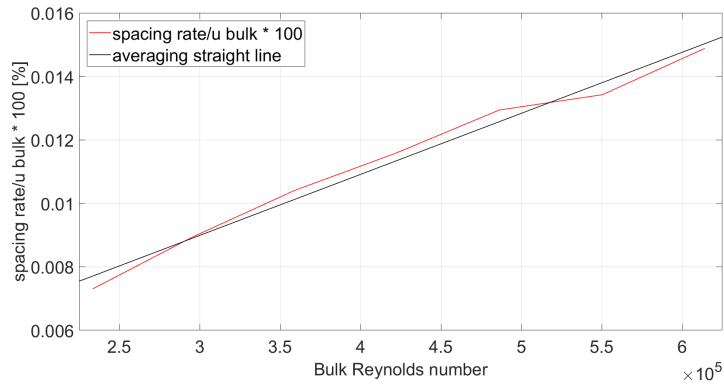


Figure 4.1: Fringe spacing rate over bulk velocity percent increase with Reynolds Bulk

This plot shows how, based on the tests conducted, the spacing rate grows in percent terms with respect to the bulk velocity of the flow in the duct, as the Reynolds number grows larger. This was viable, because all the experiments were carried using the same $50cSt$ oil. Through the use of an averaging degree 1 polynomial, it was possible to estimate a slight percent growth of around 0.0019 every 10^5 step in Re_{bulk} .

5 Conclusions

OFI measurements represent a reference point in the field of aerodynamic skin friction retrieval. They are quick, sure, when no external factors interfere, and apply to all possible flow conditions. They are hardly invasive for the flow and, as largely discussed in this thesis, practical possibilities currently exist for carrying them out over three-dimensional surfaces.

After discussing the importance of obtaining accurate skin friction measurements, a first method for implementing the OFI technique over flat geometries was presented in detail. Then, the focus of the thesis shifted towards finding a way of making fast OFI measurements over arbitrary, not a priori known, geometries possible. An alternative technique, presented in Gluzman et al. (2022), was thus carefully inspected. After which, the information learnt from the study of the two methodologies were gathered together and the obtained theoretical outcomes were used for elaborating a set of available OFI data through a newly developed code capable of assessing skin friction over arbitrary geometries and some results could be derived.

Unfortunately, in this case, OFI tests could not be carried out over surfaces with non null curvature and the algorithm developed for such an analysis remained mainly untested.

Nonetheless, OFI results were achieved for different bulk Reynolds number values, showing discrete and partially very good agreement with empirical curves and data available in the scientific literature.

References

- Dong, H., Liu, S., Geng, X., Cui, Y., and Khoo, B. (2018). A note on flow characterization of the fx63-137 airfoil at low reynolds number using oil-film interferometry technique. *Physics of Fluids*, 30(10).
- Driver, D. M. (2003). Application of oil-film interferometry skin-friction measurement to large wind tunnels. *Experiments in fluids*, 34:717–725.
- Gluzman, I., Gray, P., Mejia, K., Corke, T. C., and Thomas, F. O. (2022). A simplified photogrammetry procedure in oil-film interferometry for accurate skin-friction measurement over arbitrary geometries. *Experiments in Fluids*, 63(7):118.
- Liu, T. (2019). Global skin friction measurements and interpretation. *Progress in Aerospace Sciences*, 111:100584.
- McKeon, B., Zagarola, M., and Smits, A. (2005). A new friction factor relationship for fully developed pipe flow. *Journal of fluid mechanics*, 538:429–443.
- Monson, D. J., Mateer, G. G., and Menter, F. R. (1993). Boundary-layer transition and global skin friction measurement with an oil-fringe imaging technique. *SAE Transactions*, pages 1829–1843.
- Naughton, J. W., Viken, S., and Greenblatt, D. (2006). Skin friction measurements on the nasa hump model. *AIAA journal*, 44(6):1255–1265.
- Squire, L. C. (1961). The motion of a thin oil sheet under the steady boundary layer on a body. *Journal of Fluid Mechanics*, 11(2):161–179.
- Tanner, L. and Blows, L. (1976). A study of the motion of oil films on surfaces in air flow, with application to the measurement of skin friction. *Journal of Physics E: Scientific Instruments*, 9(3):194.
- Vinuesa, R., Örlü, R., Discetti, S., and Ianiro, A. (2017). Measurement of wall shear stress. *Experimental Aerodynamics*, pages 393–428.
- Von Karman, T. (1934). Turbulence and skin friction. *Journal of the Aeronautical Sciences*, 1(1):1–20.

- Wadcock, A. J., Yamauchi, G. K., and Driver, D. M. (1999). Skin friction measurements on a hovering full-scale tilt rotor. *Journal of the American Helicopter Society*, 44(4):312–319.
- Zanoun, E.-S., Egbers, C., Nagib, H., Durst, F., Bellani, G., and Talamelli, A. (2021). Wall friction relations in wall-bounded shear flows. *European Journal of Mechanics-B/Fluids*, 89:171–179.

